Bacterial flagellar bundling and unbundling via polymorphic transformations

Wanho Lee, Yongsam Kim, Boyce E. Griffith, and Sookkyung Lim

Bacterial flagellar bundling and unbundling via polymorphic transformations

Wanho Lee

National Institute for Mathematical Sciences,

Yuseong-gu, Daejeon 34047, Republic of Korea

Yongsam Kim

Department of Mathematics, Chung-Ang University,

Dongjakgu, Seoul 06974, Republic of Korea

Boyce E. Griffith

Departments of Mathematics, Applied Physical Sciences, and Biomedical Engineering,

Carolina Center for Interdisciplinary Applied Mathematics, and McAllister Heart Institute,

University of North Carolina, Chapel Hill, NC 27599, USA

Sookkyung Lim*

Department of Mathematical Sciences,

University of Cincinnati, Cincinnati, OH 45221, USA

Abstract

Multi-flagellated bacteria such as *E. coli* exploit the polymorphic transformations of helical flagella to explore their fluid environment. In these bacteria, a sequence of polymorphic helical forms appears consecutively as the cell 'runs' and 'tumbles.' During a run, the molecular motors that drive the twirling flagella spin counter-clockwise, and the flagella form a normal flagellar bundle. Reversing one or more of these motors, from counterclockwise to clockwise, initiates a tumble by inducing shape transformations of the associated filaments, from normal to semicoiled and then to curly 1 forms. The next run begins when the motors switch back to counterclockwise rotations. This causes the flagella to revert from curly 1 back to normal forms. This paper investigates the dynamics of elastic flagella when one or two flagella undergo a full cycle of polymorphic transformations using a computational method in which the flagellar motors are tethered in space and connected via flexible hooks to the filaments. We describe the flagellar filaments and their hooks as elastic rods adopting Kirchhoff rod theory, and their hydrodynamic interaction using a generalization of the method of regularized Stokeslets. We also investigate the role of a compliant hook in flagellar bundling.

---

* sookkyung.lim@uc.edu

I. INTRODUCTION

The flagellar bundling and unbundling processes of peritrichous bacteria such as *E. coli* and *S. typhimurium* play an important role in bacterial swimming. When all motors turn counterclockwise (CCW), a normal flagellar bundle forms and pushes the cell body to move steadily forward. This is called a *run*. Flagella unbundle when some of the motors reverse direction, leading to a *tumble* and a change in the swimming course of the cell [1–3]. During a tumble, the filaments whose motors turn clockwise (CW) transform their helical shape from normal to semicoiled and then to curly 1, which makes the cell ready for a new trajectory. Consecutively, those filaments switch their motors back to CCW, go through a transformation into the normal state, and join the bundle again for the run in a new direction. Different helical forms differ by helical pitch, helical radius, and chirality. Runs typically last about 1 s on average, and tumbles are brief events lasting about 0.1 s on average [3].

Flagellar motors drive the twirling motions of the filaments, which are linked to the motors by a flexible structure called the hook. The hook is 50-80 nm in length [4–6] and translates torque from the motor, through bends of up to $90°$, to the filament, resulting in the rotation of the long filament that participates in bundle formation. In *E. coli* swimming, hook compliance is known to be essential for flagellar bundling [7, 8].

Polymorphic transitions between different helical forms can result from external forces and hydrodynamic torque [1, 9, 10] as well as changes in solvent conditions [11–15]. Computational and theoretical studies on polymorphic transformations of flagella began many decades ago. Calladine [16–18] first presented a geometric model based on previous work by Asakura [19] and predicted 12 helical forms. Darnton *et al.* [1] subsequently used experimental data to parameterize Calladine's model. There also have been studies to understand polymorphic transitions through force-extension curves [1]. Wada and Netz [20] introduced a hybrid Brownian dynamics-Monte Carlo simulation to describe a helix that undergoes force-induced shape transformations. Similarly, Vogel and Stark [21] developed an elastic model for a flagellum based on Kirchhoff theory and coupled it to a fluid by resistive force theory. They used Brownian dynamics simulations to reproduce the experimentally characterized force-extension curves. Later, Vogel and Stark [22] proposed a continuum model of a single flagellum to describe polymorphic transformations in response to an applied motor torque as a function of time. This model demonstrates a normal-to-curly 1 transition for a single-flagellated *E. coli*, but two other intermediate states, coiled and

3

semicoiled, were only visible at the boundary between the normal and curly 1 forms.

Another approach to achieve a polymorphic transition is for the energy potential of the filament to incorporate a double-well potential, either for stretching or twisting. Srigiriraju *et al.* [23] proposed a coarse-grained continuum rod model for polymorphism in bacterial flagella that reflects the essential mechanical properties of protein subunits with a double-well potential for stretching. Goldstein *et al.* [24] developed a simple elasticity theory for a bistable helix that competes between two locally stable helical states of opposite chirality. They introduced a fully intrinsic energy formulation with two stable twist states and described the front solutions linking helical states. Both of these initial studies on polymorphism ignored the fluid environment, however. Coombs *et al.* [25] proposed a theory for the dynamics of a bistable helix under Hotani's flow environment [9], in which a rigid helix is placed in a steady flow. All previous studies on polymorphic transformations above, however, do not consider a flexible hook in the model. Recently, Ko *et al.* [26] constructed a mathematical model of a bistable helix with a double-well potential for twisting. The helical flagellum consists of a rotary motor, a flexible hook and a filament. This model, when compared to experimental data [3, 9], confirms two mechanisms for polymorphic transformations triggered by either a motor reversal or hydrodynamic torque above a certain threshold. The latter is also compared with the theoretical results [25].

In this paper, we consider both isolated and multiple flagella whose motors are tethered in space and connected via compliant hook(s) to the filament(s). Each flagellum is described by an elastic rod based on Kirchhoff rod theory, and its hydrodynamic interaction is described by a generalization of the method of regularized Stokeslets. The sequence of transformations, from normal to semicoiled to curly 1 and then to normal, that is typically observed in a real microorganism as a cyclic event is prescribed to one or several designated flagella, unlike the previous studies that consider only two states of polymorphisms. Using this model, we investigate the hydrodynamics of a single flagellum going through multi-states of polymorphic transitions and the role of the flexible hook in flagellar bundle formation with multiple flagella.

4
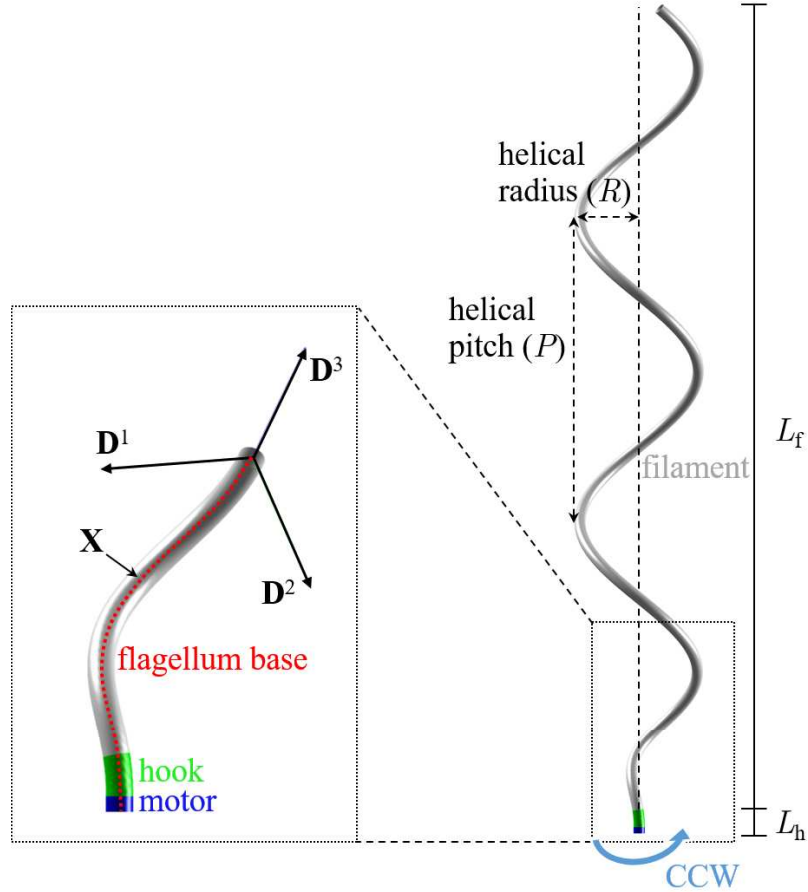
FIG. 1. (Color online) Schematic of a computational model for a single flagellum. The helical flagellar filament is linked to a compliant hook which is then linked to a rotary motor that is tethered in space and turns either counterclockwise (CCW) or clockwise (CW) at a prescribed rotational frequency. The inset shows the centerline of a helical rod $\mathbf{X}$ with an orthonormal triad $\{\mathbf{D}^1, \mathbf{D}^2, \mathbf{D}^3\}$.

II. MATHEMATICAL MODEL

A. Flagellum model by Kirchhoff rod theory

Flagella of *E. coli* are long, thin, filamentous structures that can be modeled as thin elastic rods. The flagellar filaments are typically 5–10 μm in length, but only about 20 nm in diameter. For simplicity, we introduce a single flagellum model based on Kirchhoff rod theory and apply the same approach to any additional flagella in this paper. Kirchhoff rod theory uses a space curve $\mathbf{X}(s, t)$ and its associated orthonormal triad $\mathbf{D}^i(s, t)$, $i = 1, 2, 3$, to describe the centerline of the flagellum and the degree of both bending and twisting of the flagellum; see Fig. 1. Here, t is time

5

and s is arc length along the rod in its reference configuration with $0 \leq s \leq L_{\mathrm{h}} + L_{\mathrm{f}}$, in which L_{h} and L_{f} are the lengths of the short hook and the long filament, respectively. The helical filament together with a hook is initialized as [27]:

$$\mathbf{X}(s,0) = (r(s)\cos(\alpha s), r(s)\sin(\alpha s), s), \tag{1}$$

in which α is the wave number, and the helical radius $r(s)$ is

$$r(s) = \begin{cases} 0 & , \quad 0 \leq s \leq L_{\mathrm{h}} \\ R\left(1 - e^{-c(s-L_{\mathrm{h}})^2}\right) & , \quad L_{\mathrm{h}} \leq s \leq L_{\mathrm{h}} + L_{\mathrm{f}}, \end{cases} \tag{2}$$

in which c is a constant. The helical radius is 0 for the hook ($0 \leq s \leq L_{\mathrm{h}}$), which corresponds to a straight rod, and then increases gradually to the value R for the helical filament ($L_{\mathrm{h}} \leq s \leq L_{\mathrm{h}} + L_{\mathrm{f}}$). We choose $c = 2$, so that the majority of the filament model has approximately a constant helical radius R. The value of R is determined by a polymorphic form that the flagellum takes; see Table I.

The vector $\mathbf{D}^3$ is initially defined as a unit tangent vector to the flagellum [27], and the other two vectors, $\mathbf{D}^1$ and $\mathbf{D}^2$, are perpendicular to the tangent vector following the right-hand rule, i.e., normal and binormal vectors to the flagellum. Note that the initial configuration of the flagellum given by (1) and (2) is in equilibrium in the absence of external forces, and that its deformation from the reference configuration increases internal energy and resultant force.

A flagellar motor is attached to the bottom end of the clamped hook. This motor is considered to be tethered in space at $\mathbf{X}_{\mathrm{mot}}(t) = \mathbf{X}(0,0)$ and turns either CW or CCW at a prescribed angular frequency ω. We can model the motor rotation by setting the orthonormal triad at the motor point via

$$\mathbf{D}^1_{\mathrm{mot}}(t) = (\cos(2\pi\omega t), -\sin(2\pi\omega t), 0), \tag{3}$$

$$\mathbf{D}^2_{\mathrm{mot}}(t) = (\sin(2\pi\omega t), \cos(2\pi\omega t), 0), \tag{4}$$

$$\mathbf{D}^3_{\mathrm{mot}}(t) = (0, 0, 1), \tag{5}$$

in which t is the time in seconds and ω is the rotation rate in Hz. The sign of ω determines the direction of rotation, i.e., $\omega > 0$ corresponds to CCW rotation and $\omega < 0$ corresponds to CW rotation when the rod is viewed towards the motor from the helical filament. The rotation of the motor generates torque that is transmitted to the flagellar filament through a compliant hook and eventually rotates the whole flagellum.

To describe force and torque generation by the filament, let $\mathbf{F}(s, t)$ and $\mathbf{N}(s, t)$ be the force and the moment, respectively, that are transmitted across a section of the rod at the Lagrangian coordinate s at time t. Let $\mathbf{f}(s, t)$ and $\mathbf{n}(s, t)$ be the applied force and the torque densities, respectively. Then the momentum and angular momentum balance equations are:

$$0 = \mathbf{f} + \frac{\partial \mathbf{F}}{\partial s}, \tag{6}$$

$$0 = \mathbf{n} + \frac{\partial \mathbf{N}}{\partial s} + \left(\frac{\partial \mathbf{X}}{\partial s} \times \mathbf{F} \right), \tag{7}$$

in which all the variables may be expanded in the basis of the orthonormal triad via:

$$\mathbf{F} = \sum_{i=1}^{3} F_i \mathbf{D}^i, \quad \mathbf{N} = \sum_{i=1}^{3} N_i \mathbf{D}^i, \quad \mathbf{f} = \sum_{i=1}^{3} f_i \mathbf{D}^i, \quad \mathbf{n} = \sum_{i=1}^{3} n_i \mathbf{D}^i. \tag{8}$$

The constitutive relations are given by

$$N_i = a_i \left(\frac{\partial \mathbf{D}^j}{\partial s} \cdot \mathbf{D}^k - \Omega_i \right), \tag{9}$$

in which (i, j, k) is any cyclic permutation of $(1, 2, 3)$, and

$$F_i = b_i \left(\mathbf{D}^i \cdot \frac{\partial \mathbf{X}}{\partial s} - \delta_{3i} \right), i = 1, 2, 3, \tag{10}$$

in which δ_{3i} is the Kronecker delta. The coefficients a_1 and a_2 are the bending moduli, and a_3 is the twist modulus of the rod. The coefficients b_1 and b_2 are the shear moduli, and b_3 is the stretching modulus that controls the degree of the inextensibility of the rod. The strain twist vector $(\Omega_1, \Omega_2, \Omega_3)$ designates the intrinsic properties of the elastic rod, in which $\kappa \equiv \sqrt{\Omega_1^2 + \Omega_2^2}$ is the intrinsic curvature, and $\Omega_3 \equiv \tau$ is the intrinsic twist of the rod. The sign of τ determines the helical handedness of the rod. Negative values of τ correspond to a left-handed helix and positive values of τ correspond to a right-handed helix. The constitutive relations above can be derived from a variational argument of the elastic energy potential for the unconstrained version of the Kirchhoff rod model [28],

$$E = \frac{1}{2} \int_0^L \left[\sum_{i=1}^{3} a_i \left(\frac{\partial \mathbf{D}^j}{\partial s} \cdot \mathbf{D}^k - \Omega_i \right)^2 + \sum_{i=1}^{3} b_i \left(\mathbf{D}^i \cdot \frac{\partial \mathbf{X}}{\partial s} - \delta_{3i} \right)^2 \right] ds, \tag{11}$$

in which $L = L_{\mathrm{h}} + L_{\mathrm{f}}$ is the total length of the rod and (i, j, k) is any cyclic permutation of $(1,2,3)$. Note that, in the limit $b_3 \to \infty$, the rod becomes completely inextensible. In this work, we choose b_3 to be sufficiently large to make the rod almost inextensible, and we set $a_1 = a_2$ so that the rod is isotropic. The intrinsic curvature and twist, κ and τ, will vary with s and t as the flagellum transforms from one polymorphic form to another.

TABLE I. Geometric properties of polymorphic forms.

Polymorphic form	Pitch (P)	Radius (R)	Curvature (κ_0)	Twist (τ_0)
Normal (left-handed)	2.1611 μm	0.2161 μm	$\kappa_0^n = 1.3097$	$\tau_0^n = -2.0845$
Semicoiled (right-handed)	1.0766 μm	0.3810 μm	$\kappa_0^s = 2.1831$	$\tau_0^s = 0.9818$
Curly 1 (right-handed)	1.3199 μm	0.1975 μm	$\kappa_0^c = 2.3757$	$\tau_0^c = 2.5268$

B. Modeling polymorphic transformations of a flagellum

Bacterial flagella can take on various polymorphic forms that have different helical pitches, helical radii and handedness, and they can transform from one polymorphic form to another [1, 3]. Table I lists the geometric properties of typical polymorphic forms, and Fig. 2 shows their configurations in the equilibrium states. As a cell runs, all of its motors turn CCW, and all of its flagella adopt a normal left-handed form. When at least one of the motors switches its direction from CCW to CW, a kink appears at the motor end and propagates to the proximal end along the flagellum by transforming the flagellum from a normal state to a *semicoiled* right-handed state, and then another kink appears and the flagellum transforms from semicoiled to a *curly 1* right-handed state. When the motor turns back to CCW rotation, the flagellum returns back to the normal form.

To model a sequence of polymorphic transformations, we use experimental data on helical pitch (P) and radius (R) of different polymorphic forms by converting them into intrinsic curvature (κ_0) and twist (τ_0) via [20, 29]

$$\kappa_0 = \frac{R}{R^2 + (P/(2\pi))^2},$$
$$\tau_0 = H\frac{P}{2\pi(R^2 + (P/(2\pi))^2)},$$

in which H is handedness, with $H = -1$ for a left-handed helix and $H = 1$ for a right-handed helix.

Because our helical shape is motivated by Higdon [27], the intrinsic curvature and twist of each polymorphic form are functions of the variable s and can be computed directly using Eqs. (1-2). Let us denote by $\kappa^n(s)$ and $\tau^n(s)$ the intrinsic curvature and twist of the normal flagellum, respectively. The polymorphic transformation involves their changes in time as the flagellum is in the process of transformations, which is done by prescribing the variable twist $\tau(s, t)$ in the
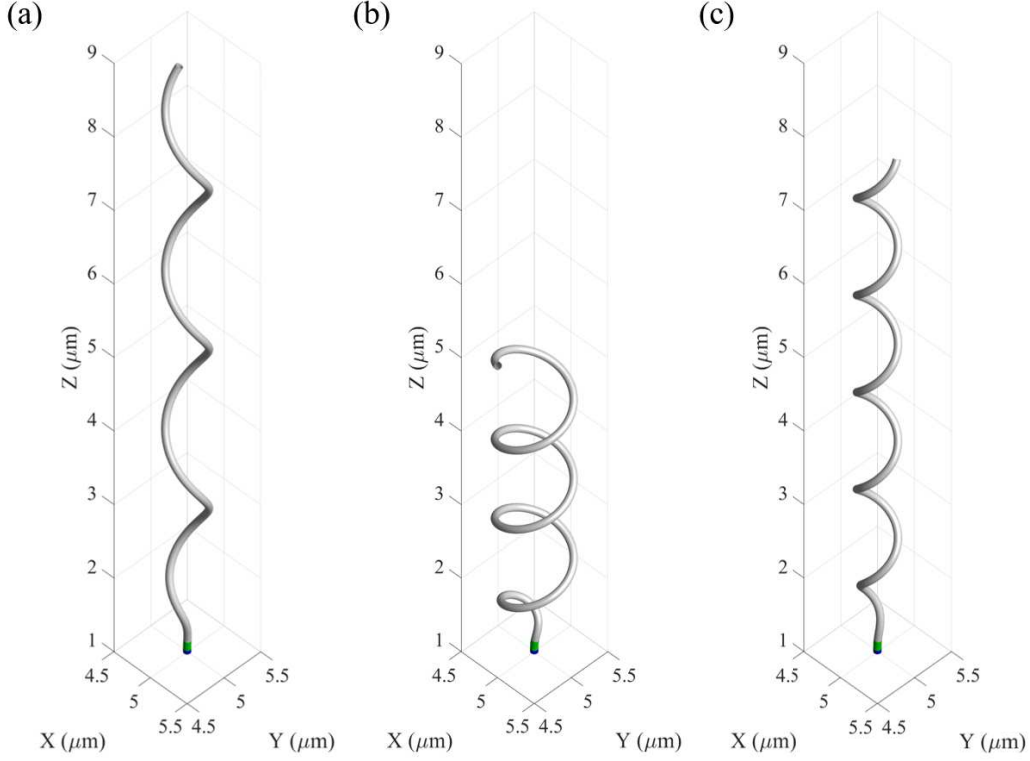
FIG. 2. Equilibrated configurations of the (a) normal, (b) semicoiled, and (c) curly 1 flagella determined by the geometric properties given in Table I.

following form:

$$
\tau(s,t) =
\begin{cases}
\tau^{\mathrm{n}}(s) & \text{if } t - \frac{s}{v_{\mathrm{k}}} \leq t_{\mathrm{ns}}, \\[2mm]
(\tau_0^{\mathrm{s}}/\tau_0^{\mathrm{n}}) \times \tau^{\mathrm{n}}(s) & \text{if } t_{\mathrm{ns}} < t - \frac{s}{v_{\mathrm{k}}} \leq t_{\mathrm{sc}}, \\[2mm]
(\tau_0^{\mathrm{c}}/\tau_0^{\mathrm{n}}) \times \tau^{\mathrm{n}}(s) & \text{if } t_{\mathrm{sc}} < t - \frac{s}{v_{\mathrm{k}}} \leq t_{\mathrm{cn}}, \\[2mm]
\tau^{\mathrm{n}}(s) & \text{if } t_{\mathrm{cn}} < t - \frac{s}{v_{\mathrm{k}}},
\end{cases}
$$

in which v_{k} is the kink velocity along the flagellum, and t_{ns}, t_{sc}, t_{cn} represent the time when semi-coiled, curly 1, and normal states start, respectively. The variable curvature, $\kappa(s,t)$, is prescribed similarly. An *E. coli* cell typically rotates its motors around 100 Hz and tumbles in the time duration ~ 0.1 s [2, 3]. Since the filament length is 9 μm, we choose $v_{\mathrm{k}} = 90$ μm/s so that the kink takes 0.1 s to propagate along the flagellum. It is reported *in silico* that the kink speed is linearly proportional to the motor rotation rate [26].

We assume that there is neither more than one kink along the flagellum nor a gap between two consecutive kinks. Thus $t_{\mathrm{sc}} - t_{\mathrm{ns}}$ and $t_{\mathrm{cn}} - t_{\mathrm{sc}}$ are both 0.1 s. Figure 3 shows a schematic diagram
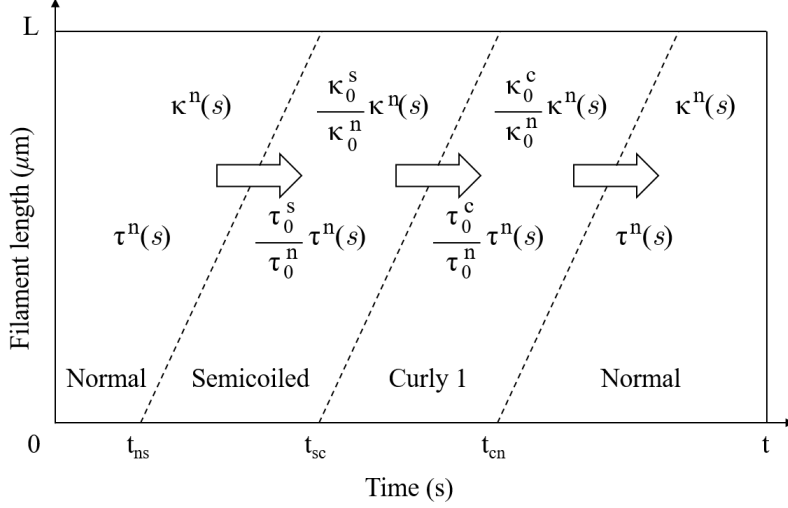
FIG. 3. A schematic diagram of prescribed changes in intrinsic curvature and twist along a flagellum during one cycle of polymorphic transformations.

of changes in intrinsic curvature and twist along the flagellum over time when the flagellum transitions from normal to semicoiled and to curly 1. The dotted line separating the two different states indicates the time and position of the kink on the flagellum.

C. Generalized method of regularized Stokeslets

A single or multiple flagella, whose rotary motors are tethered in space, are immersed in a viscous fluid that is governed by the incompressible Stokes equations with regularized forcing along the filament [30, 31]

$$0 = -\nabla p + \mu \Delta \mathbf{u} + \mathbf{g}, \tag{12}$$

$$0 = \nabla \cdot \mathbf{u}, \tag{13}$$

in which μ is the fluid viscosity. The unknown variables $\mathbf{u}(\mathbf{x}, t)$, $p(\mathbf{x}, t)$, and $\mathbf{g}(\mathbf{x}, t)$ are the fluid velocity, fluid pressure, and the external force per unit volume applied to the fluid, respectively, where $\mathbf{x}$ are fixed physical coordinates. The force density $\mathbf{g}$ in Eq. (12), generated by the deformation of the rotating elastic flagella, is given by

$$\mathbf{g}(\mathbf{x}, t) = \int_0^L (-\mathbf{f}(s, t))\psi_\epsilon(\mathbf{x} - \mathbf{X}(s, t))ds + \frac{1}{2}\nabla \times \int_0^L (-\mathbf{n}(s, t))\psi_\epsilon(\mathbf{x} - \mathbf{X}(s, t))ds$$
$$+ \int_0^L (-\mathbf{f}^r(s, t))\psi_\epsilon(\mathbf{x} - \mathbf{X}(s, t))ds, \tag{14}$$

10

where the blob function ψ_ϵ used in this study is

$$\psi_\epsilon(\mathbf{r}) = \frac{15\epsilon^4}{8\pi(|\mathbf{r}|^2 + \epsilon^2)^{7/2}}, \tag{15}$$

in which ϵ is the regularization parameter and $\mathbf{r} = \mathbf{x} - \mathbf{X}$ for a point $\mathbf{x}$ in the fluid [30, 31]. The blob function ψ_ϵ is a radially symmetric bell-shaped function with infinite support and satisfies $\iiint_{\mathbf{R}^3} \psi_\epsilon(\mathbf{r}) \, d\mathbf{r} = 1$. It is designed to spread most of the force and moment within a ball of radius ϵ centered at the point of application on the rod. Eq. (14) describes how we apply the force and torque generated in the flagella to the fluid, and this implies that the rate at which the immersed body works on the fluid is written in terms of the force and moment applied to the fluid [28, 32].

In Eq. (14), $\mathbf{f}^{\mathrm{r}}(s, t)$ is the repulsive force that is added both to prevent penetration between flagella and also to facilitate unbundling. Let s and s' be any two material points on different flagellar filaments. The repulsive force between the material points is

$$\mathbf{f}^{\mathrm{r}}(s, t) = \begin{cases} C_{\mathrm{s}} \left(1 - \frac{|\mathbf{X}(s,t) - \mathbf{X}(s',t)|}{D_{\mathrm{m}}} \right) \frac{\mathbf{X}(s,t) - \mathbf{X}(s',t)}{|\mathbf{X}(s,t) - \mathbf{X}(s',t)|} & \text{if } |\mathbf{X}(s, t) - \mathbf{X}(s', t)| \leq D_{\mathrm{m}}, \\ 0 & \text{otherwise,} \end{cases}$$

in which C_{s} is the stiffness constant and D_{m} is the minimum distance allowed between two flagella.

Together with Eqs. (6)-(10) and (12)-(14), the coupled system of equations closes with the addition of the following equations:

$$\mathbf{w}(\mathbf{x}, t) = \frac{1}{2} \nabla \times \mathbf{u}(\mathbf{x}, t), \tag{16}$$

$$\frac{\partial \mathbf{X}(s, t)}{\partial t} = \mathbf{u}(\mathbf{X}(s, t), t) - \frac{1}{\alpha} \left(\mathbf{f}(s, t) + \mathbf{f}^{\mathrm{r}}(s, t) \right), \tag{17}$$

$$\frac{\partial \mathbf{D}^i(s, t)}{\partial t} = \mathbf{w}(\mathbf{X}(s, t), t) \times \mathbf{D}^i(s, t), i = 1, 2, 3. \tag{18}$$

Eq. (16) is the relation between the angular and linear fluid velocities, $\mathbf{w}$ and $\mathbf{u}$, that are both solved using a regularized Stokes formulation [30, 31]. The interaction between the elastic rod and the fluid is described in Eqs. (17) and (18). Whereas the triad rotates at the local fluid angular velocity by the no-slip condition, the centerline of the rod translates at the local fluid velocity with a correction for relative slip between boundary and fluid by an amount proportional to the boundary force. This relative slip is added to allow for a smooth slip between two close flagella [32]. See [31, 33] for a more detailed description of both the mathematical formulation and its numerical scheme.

TABLE II. *Computational and physical parameters*

Parameters (symbol)	Value
Fluid viscosity (μ)	0.01×10^{-4} g/(μms)
Mesh width for flagellum (Δs)	$0.03\,\mu$m
Number of material points of the rod	301
Regularization parameter (ϵ)	$3.5\Delta s$
Time step (Δt)	$1.25 \times 10^{-7} s$
Translational drag coefficient (α)	$1/120$ g/(μms)
Stiffness for the repulsive force (c_s)	100 g/s^2
Allowed minimum distance between two flagella (D_m)	$0.08\,\mu$m
Length of filament ($L_{\rm f}$)	$9\,\mu$m
Bending modulus of filament ($a_{1,2} = a$)	0.0035 gμm^3/s^2
Twist modulus of filament (a_3)	0.0035 gμm^3/s^2
Shear modulus ($b_1 = b_2$)	0.8 gμm/s^2
Stretch modulus (b_3)	0.8 gμm/s^2
Length of hook ($L_{\rm h}$)	$0.06\,\mu$m
Bending modulus of hook ($a_{1,2}^{hook} = a^{hook} = a/20$)	0.000175 gμm^3/s^2
Twist modulus of hook ($a_3^{hook} = a_3$)	0.0035 gμm^3/s^2

Table II shows the computational and physical parameters used in this paper, in which the available values are obtained from the literature on multiple-flagellated bacteria [1, 3, 18, 34, 35]. The fluid viscosity μ is the same as that of water. Note that the length of the hook is set to be 60 nm [4–6], and the bending modulus of the hook is set equal to $1/20$ of the filament, whereas the twist modulus of the hook is kept the same as that of the filament.

III. RESULTS AND DISCUSSION

Our simulations investigate how multiple steps of polymorphic transformations affect the flagellar hydrodynamics, first with a single flagellum and then with multiple flagella. We also investigate computationally the role of hooks in flagellar bundling and unbundling which are important aspects of bacterial swimming.
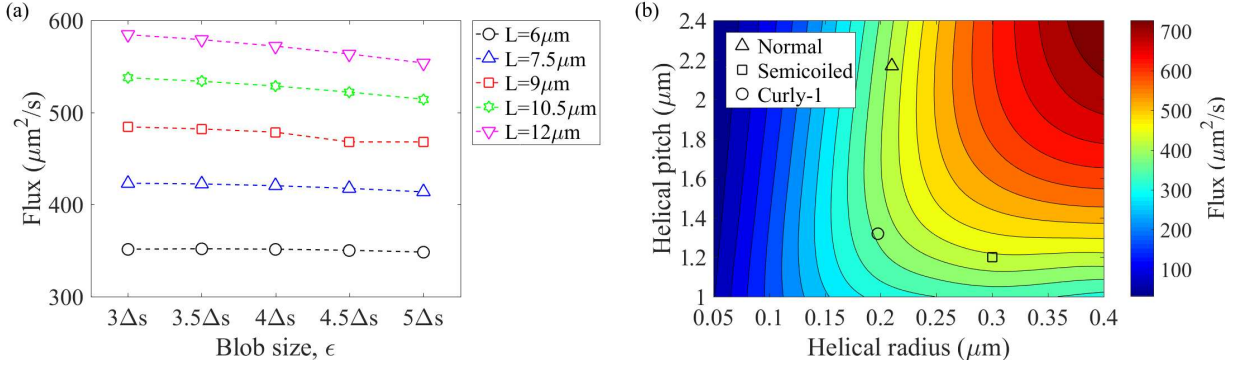
FIG. 4. (Color online) Fluxes depending on (a) various blob sizes and filament lengths and (b) helical radius and pitch when $L = 9\mu$m and $\epsilon = 3.5\Delta s$.

A. Dynamics of a single flagellum with various polymorphic forms

Before we simulate a sequence of polymorphic transformations, we study how fluid fluxes depend on the filament length L, the helical properties, and the regularization parameter ϵ in Eq. (15) that controls the effective radius of the filament. The flux generated by a rotating helical flagellum is closely related to the speed of a bacterium when it can freely move in a fluid.

Figure 4(a) displays the amount of flux as functions of the blob size for various filament lengths. A flagellar motor of the flagellum rotates CCW at the rate of 100 Hz, persisting the normal left-handed form over time, which pumps the fluid upward. Fluxes are measured after the flagellum reaches steady rotational motion. As the filament length is increased, the amount of flux tends to increase proportionally. We also see that the amount of flux decreases with the blob size, which implies that the amount of flux increases as the filament gets thinner while the filament maintains its helical pitch and radius. In our formulation, the blob size determines the effective thickness of the filament.

Figure 4(b) shows the flux contour depending on helical pitch and helical radius when $L = 9 \mu m$ and $\epsilon = 3.5\Delta s$ are held fixed. The flux generally increases as the helical radius and pitch increase. For small values of helical radii, however, the flux is almost constant, independent of the helical pitches. For larger radii, the flux is proportional to helical pitch. As the filament length varies from $L = 7.5 \mu$m to $L = 10.5 \mu$m (not shown here), we found that the overall patterns are the same. Notice the flux values, when the flagellum is of the steady form of the normal, semicoiled, and curly 1 in our model, are indicated by triangle, square, and circle, respectively.

Next we consider the effects of switching the direction of rotation from CCW to CW and vice

13

versa, inducing the sequence of polymorphic transformations that result in the change of helical pitch, helical radius, and/or handedness of the flagellum. During each polymorphic transition, a kink is initiated at the motor and propagates to the filament end. Figures 5(a)-5(e) display the time evolution of a rotating flagellum showing polymorphic changes in the order of normal (CCW, LH), semicoiled (CW, RH), curly 1 (CW, RH) and back to normal (CCW, LH), where LH stands for left-handed and RH for right-handed. (See also supplemental Movie 1.) The flagellar motor first turns CCW and the filament adopts a normal form until $t = 0.05$ s, when the motor switches to CW rotation and the flagellum transforms from normal to semicoiled. At $t = 0.15$ s, another transformation from semicoiled to curly 1 is initiated while the motor still turns CW. Last, as the motor switches from CW back to CCW at $t = 0.25$ s, the flagellum transforms from curly 1 back to normal. Note that only the change of the rotational direction leads to the change of the helical handedness. The trajectories of fluid markers distributed around the flagellum are shown in gray.

In Fig. 5 (f), we estimate the torsion ($\frac{\partial \mathbf{D}^1}{\partial s} \cdot \mathbf{D}^2$) along the flagellum over time as the flagellum undergoes a sequence of transformations. Negative values of torsion correspond to the left-handed helical section and positive values correspond to the right-handed one. Notice also the colors of the flagellum in (a)-(e) that represent the same amount of the torsion as in (f). It is clear that the kink propagated along the flagellum of which the speeds are illustrated as the slopes of the slanted curves.

In Fig. 6(a), the flux is shown as a function of time during polymorphic changes. For a rotating flagellum, there are four combinations of the helical handedness and the rotational direction, (LH, CCW), (LH, CW), (RH, CCW) and (RH, CW). It has been previously reported that only two combinations, (LH, CCW) and (RH, CW), enable the flagellum to pump the fluid upward because the helical wave driven by the motor propagates to the free end of the flagellum [32]. Therefore, the flagellum exhibits the positive flux most of the time. However, we observe substantial flow reduction, even resulting in a negative flux, generally after the motor switches the direction of rotation at $t = 0.05$ s and $t = 0.25$ s. In particular, when the polymorphic state changes from normal to semicoiled, the helical pitch is reduced approximately by a factor of two and the radius becomes larger, so that the helical axis becomes shorter as the kink runs along the flagellum, see Figs. 5(b) and 5(c). This has the momentary effect of pulling the flagellum toward the motor and causing the fluid to flow downward. One possible reason for the negative flux is that our model does not have a cell body and all motors are embedded in the same plane, which does not allow the cell to move freely. A free bacterial swimmer might always produce a positive flux because
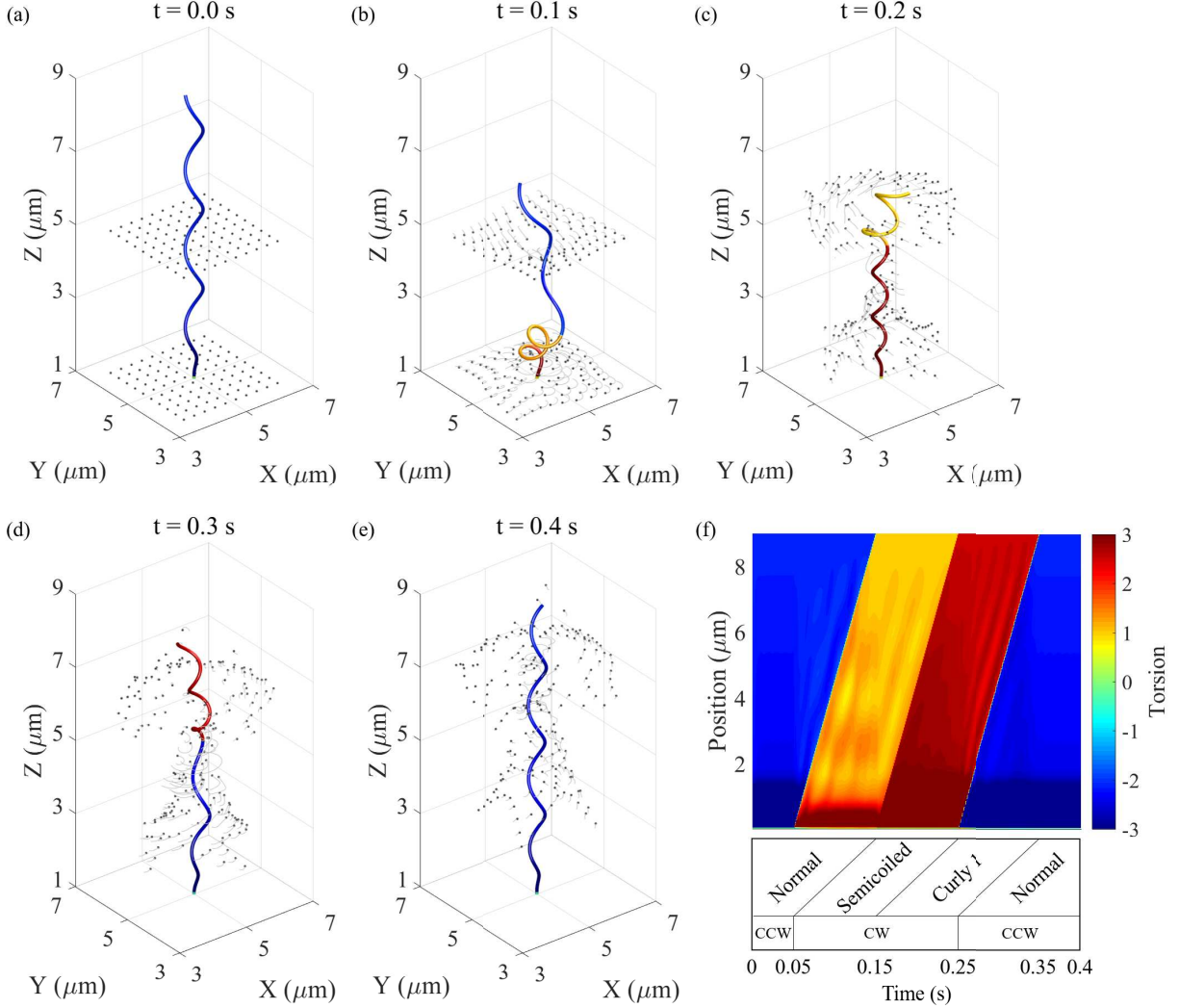
FIG. 5. (Color online) A sequence of polymorphic transformations over time together with the recent trajectories of fluid markers in gray (a-e) and their corresponding torsion (f). The filament transforms from normal to semicoiled then to curly 1 and back to normal. The torsion is calculated as $\frac{\partial \mathbf{D}^1}{\partial s} \cdot \mathbf{D}^2$ along the flagellum, indicating that the negative and positive values correspond to the left-handed and the right-handed sections of the flagellum, respectively.

the flagella take only two combinations of (LH, CCW) and (RH, CW) that generate thrust.

Figure 6(b) depicts the variation of elastic energies over time. Overall, shear and stretch energies are negligible compared to the twist and bending energies at all times. The twist energies spike at 0.05 s and 0.25 s when the direction of motor rotation changes. It is generally observed that the twist energy is large compared to the bending energy in the time interval when the normal form remains but the bending energy is dominant when the semicoiled form remains in the process

15
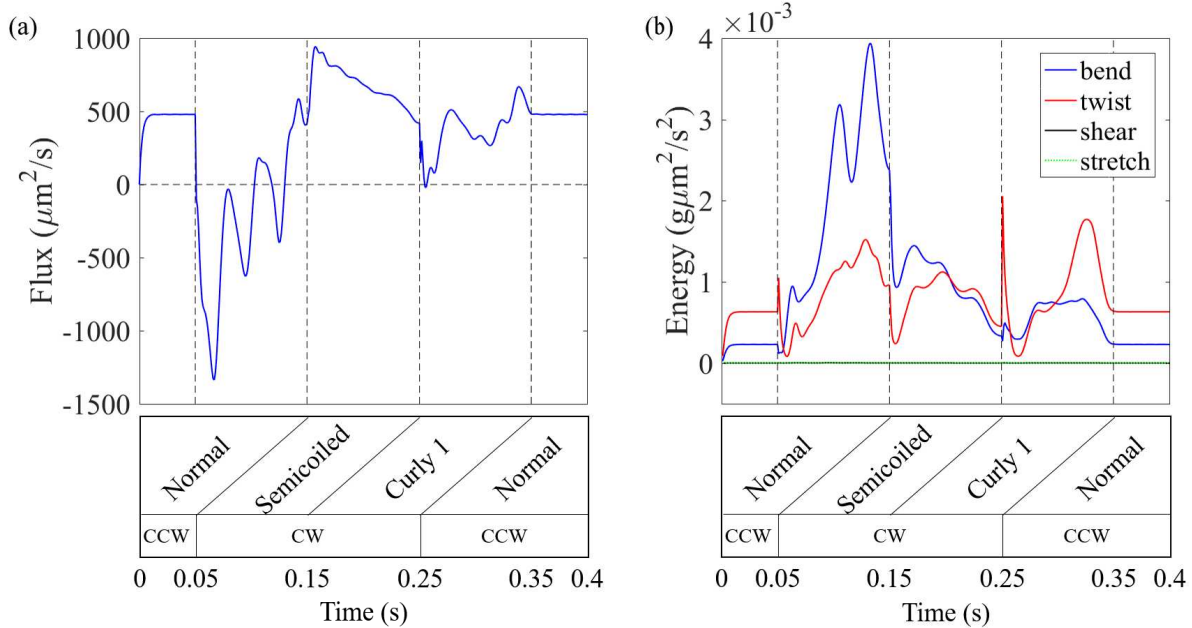
FIG. 6. (Color online) Time evolutions of (a) flux and (b) energies of a rotating flagellum as it experiences polymorphic changes.

of polymorphic changes.

To provide insight on the behavior of the energies shown in Fig. 6, we show in Fig. 7 the bending (left) and twist energies (right) generated by a rotating mono-state flagellum as the helical pitch and radius vary. For a fixed helical pitch, both bending and twist energies increase with the helical radius, and the total energy (addition of the two energies) is almost proportional to the helical radius. The bending and twist energies are approximately constants for small values of radius independent of the helical pitch. It is interesting to see that, for larger values of radius, the bending energy increases and the twist energy decreases as the helical pitch decreases. We can also see that, while the twist energy is larger than the bending energy for the mono-state normal flagellum ('triangle'), the bending energy is dominant for the semicoiled state flagellum ('square'), which maintains in the process of polymorphic changes of the flagellum, see Fig. 6(b).

B. Hydrodynamics of multiple flagella

Flagellar bundling and unbundling are essential for reorientation of bacterial cells. Bacterial flagella come together and form a bundle when all the flagella are normal and turn counterclockwise. When at least one motor reverses to CW, the associated flagellar filament leaves the bundle

16
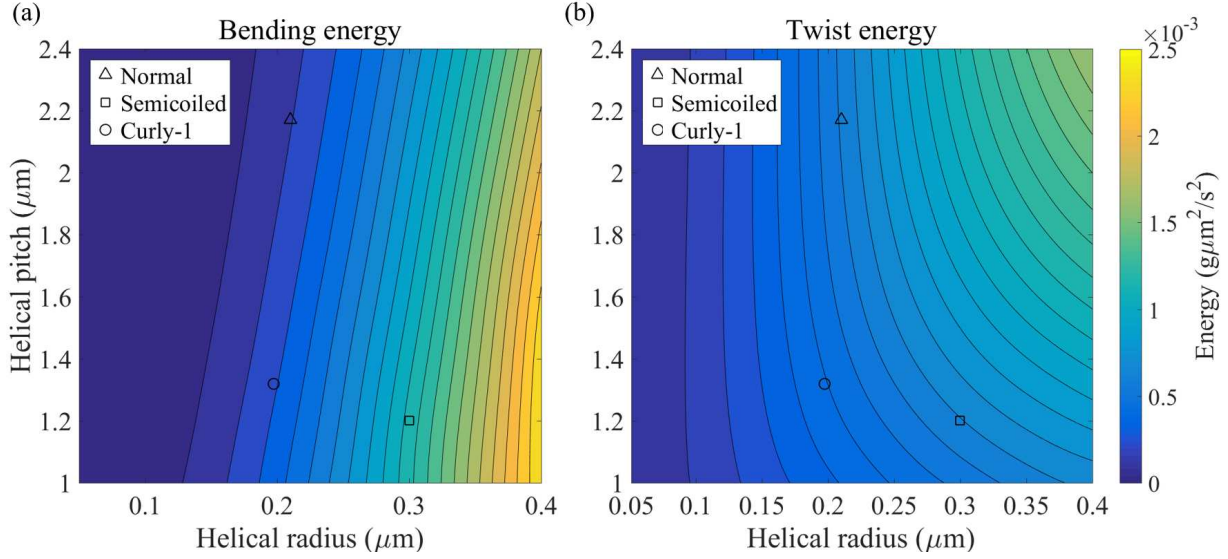
FIG. 7. (Color online) (a) Bending and (b) twist energies generated by a rotating mono-state flagellum as the helical pitch and radius vary.

while it is going through polymorphic changes, leading to unbundling.

The bundling process with multiple flagella is shown in Fig. 8, where four flagella initially stand straight with their bottom ends (motors) being equally distributed on a circle with a radius of 0.8644 μm. (See also supplemental Movie 2.) All motors turn CCW at the rate of 100 Hz, which consequently drive the rotation of the flagella CCW as well. The hydrodynamic interaction of flagella allows each flagellum's precession and brings all the flagella together to form a bundle [36], which pumps up the fluid away from the motor. The trajectories of fluid markers are shown in gray.

Figure 9 shows the fluid flux as a function of time for models with different numbers of flagella. The fluxes generated by multiple flagella are larger than that by a single flagellum at the beginning of the bundling; however, as flagellar bundling proceeds, the fluxes generated by multiple flagella become smaller than that generated by only a single flagellum. As the flagella form a bundle resulting in a superflagellum, the fluxes reach almost constant values, which decrease as the number of flagella increases. This observation is consistent with the results in Fig. 4, which shows that the flux decreases as the effective thickness of the flagellum increases. The effective thickness of the superflagellum becomes larger with more flagella and thus results in a lower flux; compare four superflagella in Fig. 9(b), which shows the snapshots at $t = 1.0$ s for bundles with $1 - 4$ flagella. It is experimentally reported that the swimming speed of a cell is similar with and without bundles,

17
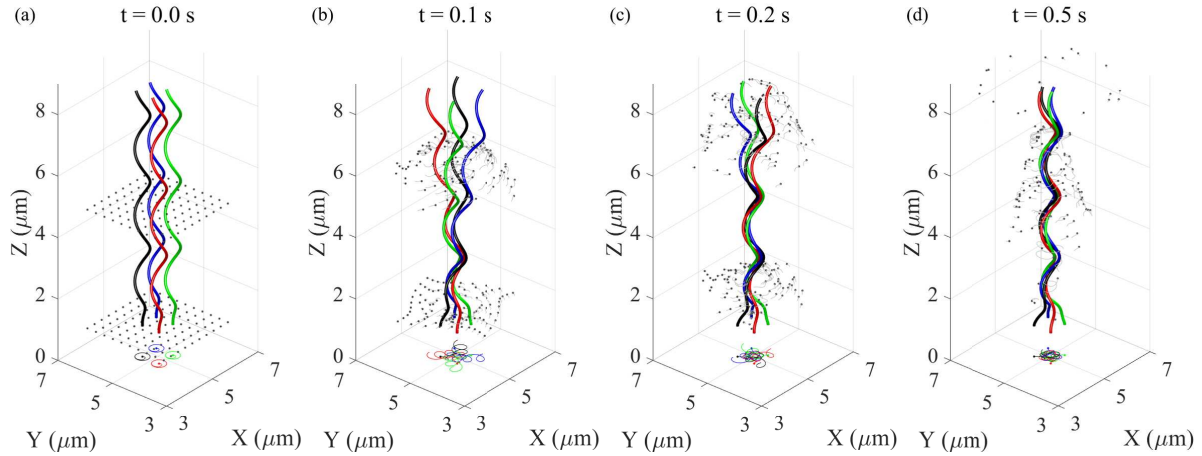
FIG. 8. (Color online) Bundling process of four rotating flagella. Each flagellum takes the normal form, and its motor rotates CCW at 100 Hz. The curves on the XY-plane are the projection of the four helices, and the fluid markers in gray are passive fluid tracers.
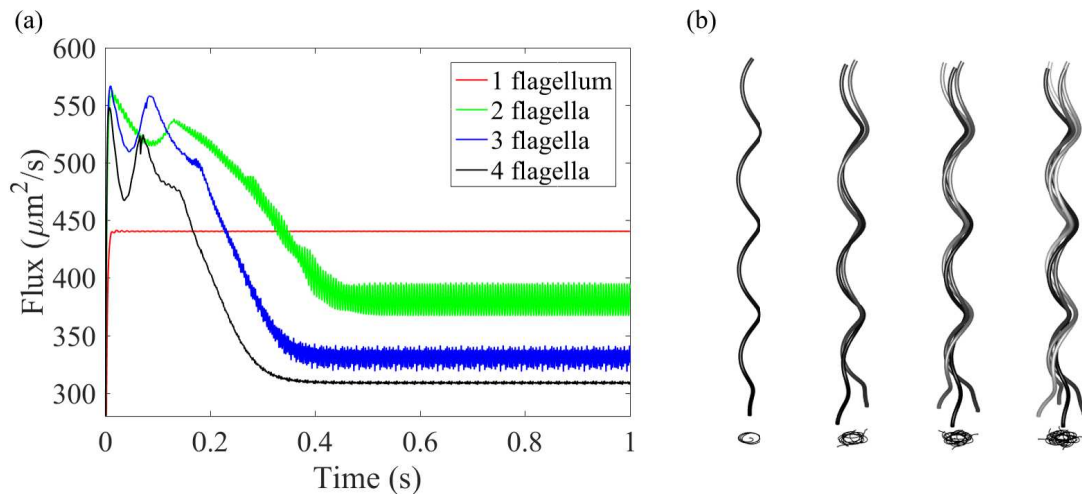
FIG. 9. (Color online) (a) Fluxes over time for 4 different numbers of flagella. The larger the number of flagella gets, the smaller the flux is after flagella complete a bundling. (b) Snapshots taken at $t = 1.0$ s for bundles with 4 different numbers of flagella.

which indicates that the role of the bundle is not to increase swimming speed. Multiple flagella may be necessary for cell's reorientation of broader spectrum since any of the motors can switch the swimming direction [8, 37].

Although a compliant hook may not play a significant role in a single flagellum alone, it becomes important when it comes to flagellar bundling with multiple flagella [38]. Figure 10 shows

18
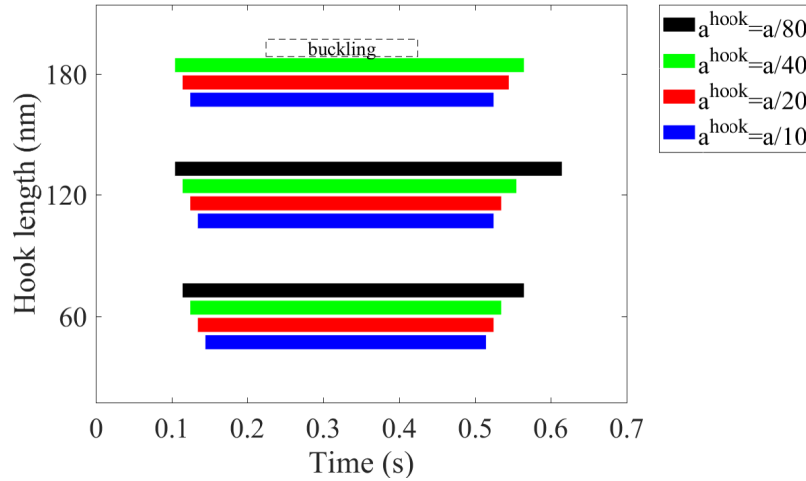
FIG. 10. (Color online) Duration of bundle formation of two flagella depending on the hook length and bending modulus of the hook.

duration of a bundle formation with two flagella is illustrated as horizontal stripes as the length and the bending modulus of the hook vary. The length of the hook is varied from 60 nm, 120 nm, to 180 nm, and the bending modulus is taken to be 1/10, 1/20, 1/40, and 1/80 times that of the filament. The two flagella initially stand in parallel. The duration of bundle formulation is measured from the time when the two flagella meet first in the close proximity within a certain range till the time when the free ends of the flagella finally enter the range. Figure 10 shows how early the flagella meet and how long it takes the flagella to complete the bundle formulation. It is generally found that as the hook length increases and as the bending modulus decreases, bundle formation begins earlier and finishes later, and thus takes more time. If the length of the hook is too long and the bending modulus is too small, the hook buckles and is unable to form a bundle, which indicates that elastic and geometric properties of the hook should be within a certain range for a proper bundling process.

Next, we investigate the bundle formation when two flagella are not in parallel, as illustrated in Fig. 11(a), which shows the initial setting of two flagella forming an angle 2ϕ. The bottom ends (motors) of the two flagella are held tethered, and the rotational axes of the two motors maintain an angle 2ϕ for all time. The length of each hook is chosen to be 60 nm. With various combinations of the initial angle between flagella and the bending modulus of the hook, we measure the distance between the tips of the flagella after the flagellar motion reaches the steady rotation; see Fig. 11(b). Here, large distance values indicate that two flagella do not bundle and rotate inde-

19
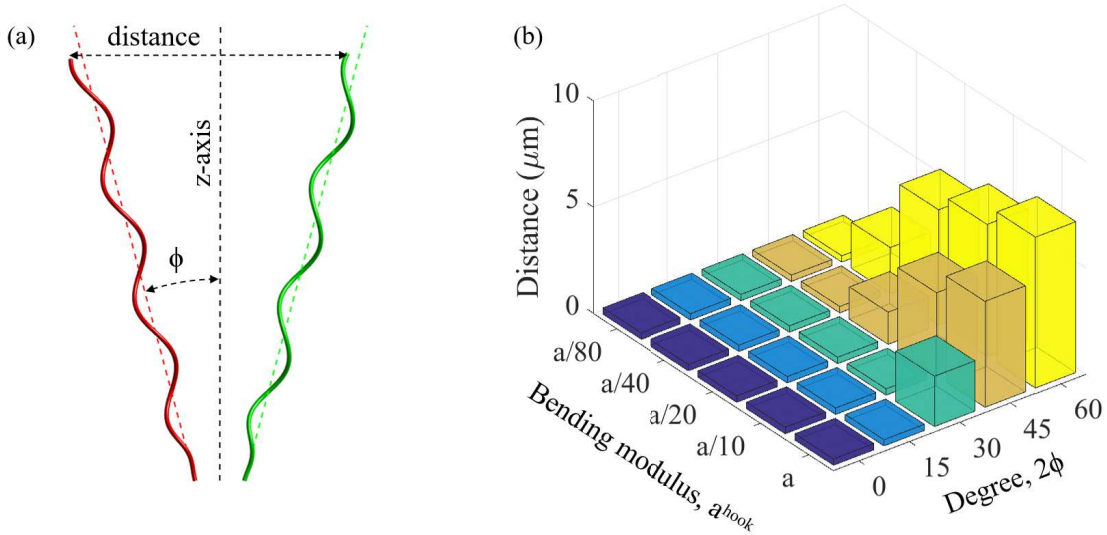
FIG. 11. (Color online) (a) Initial setting of two flagella with an angle 2ϕ and (b) distance between two ends of the flagella measured after the steady motion is reached.

pendently with some distance, whereas the values close to zero indicate that the two flagella form a bundle and rotate together. Clearly, it is difficult for flagellar bundles to form if the bending modulus of the hook is too large and the initial angle between the flagella is large. Since flagella in a real bacterium are randomly distributed over the cell body, this simulation result implies that the flexibility of the hook might be crucial in flagellar bundling. The hook can bend up to $90°$ from the axis of rotation at the motor, and it is hypothesized that the hook functions as a universal joint [7]. Recently, experiments have shown that the stiffening of the hook disrupts bundle formation, leading to atypical swimming kinematics [8].

Figure 12 shows the time evolution of the motion of four flagella when one of them, the flagellum labeled 1, goes through a sequence of polymorphic transformations, while the rest persist the normal form. (See also supplemental Movie 3.) Flagellum 4 stands in the center of the other three flagella that encircle it with $15°$ of helical axes. The colors on the flagellum 1 represent the same amount of the torsion along the flagellum as in Fig. 5(f). At the beginning, all flagella are normal and their motors turn CCW, resulting in the bundling of the flagella; see the figure at $t = 0.65$ s. The first polymorphic change of flagellum 1 from normal to semicoiled appears at $t = 0.7$ s, the second from semicoiled to curly 1 appears at $t = 0.8$ s, and the last from curly 1 to normal appears at $t = 0.9$ s. A motor reversal (CCW to CW) of the flagellum 1 initiates the first transformation and also unbundling process. Upon completing the first transformation, flagellum 1 completely

20
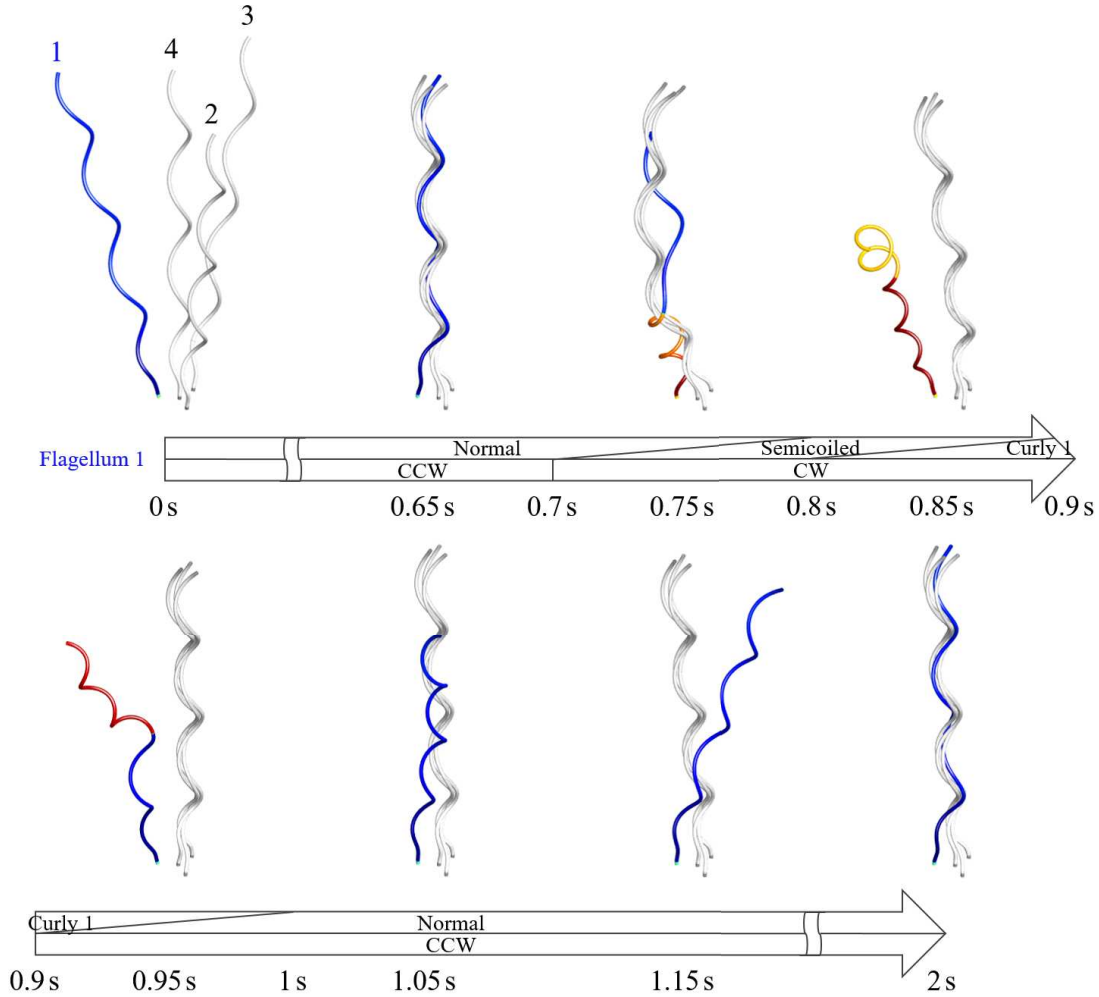
FIG. 12. (Color online) Time evolution of the motion of four rotating flagella. All the flagella are initially normal and their motors turn CCW, resulting in bundle formation. Only flagellum 1 experiences polymorphic changes and the rest keep the normal state. The first transformation from normal to semicoiled starts at $t = 0.7$ s, the second from semicoiled to curly 1 starts at $t = 0.8$ s, and the last from curly 1 back to normal starts at $t = 0.9$ s.

leaves the bundle with the others staying in bundle, which may result in reorientation of the cell body. The motor reversal of the flagellum 1 from CW to CCW allows the filament 1 to rejoin the bundle. Since all motors are tethered in space, the new bundle lies in the same direction of the first bundle, otherwise, the direction of the new bundle would have changed from the direction of the original bundle.

Figure 13 displays the time evolution of the motion of four flagella when two (flagella 1 and 4) of them go through the same sequence of polymorphic changes at the same time as the flagellum
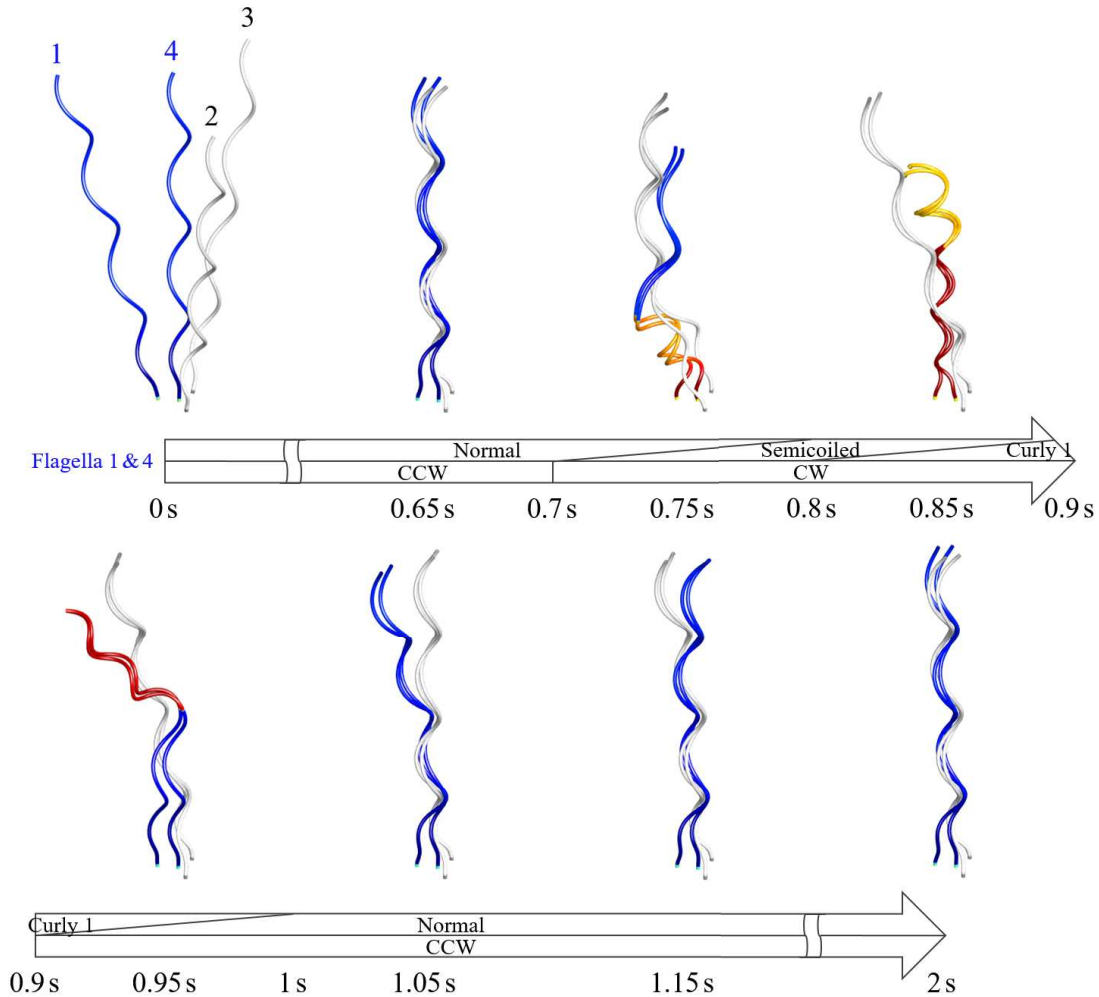
FIG. 13. (Color online) Dynamics of flagellar bundling and unbundling. All four flagella are initially normal and their motors turn CCW. Two flagella 1 and 4 experience the same sequence of polymorphic changes at the same time as the flagellum 1 in the previous case and the rest remains normal.

1 in the previous case and the rest remains normal. (See supplemental Movie 4.) Similar to the previous case, the flagella 1 and 4 leave the bundle when their motors reverse to CW and they transform from normal to semicoiled; however, there are two bundles that are made by the transformed flagella and the untransformed flagella. The motors reverse again to CCW and hence cause the curly 1 form to revert back to normal form, which enforces two sets of bundles to join together again.

To analyze more quantitatively the bundling and unbundling processes, we measure the distance from the tip of the central flagellum 4 to the tips of the flagella 1, 2, and 3; see Fig. 11(a). Figure 14 depicts the distances between tips as functions of time for the cases in Fig. 12 (left) and in Fig. 13
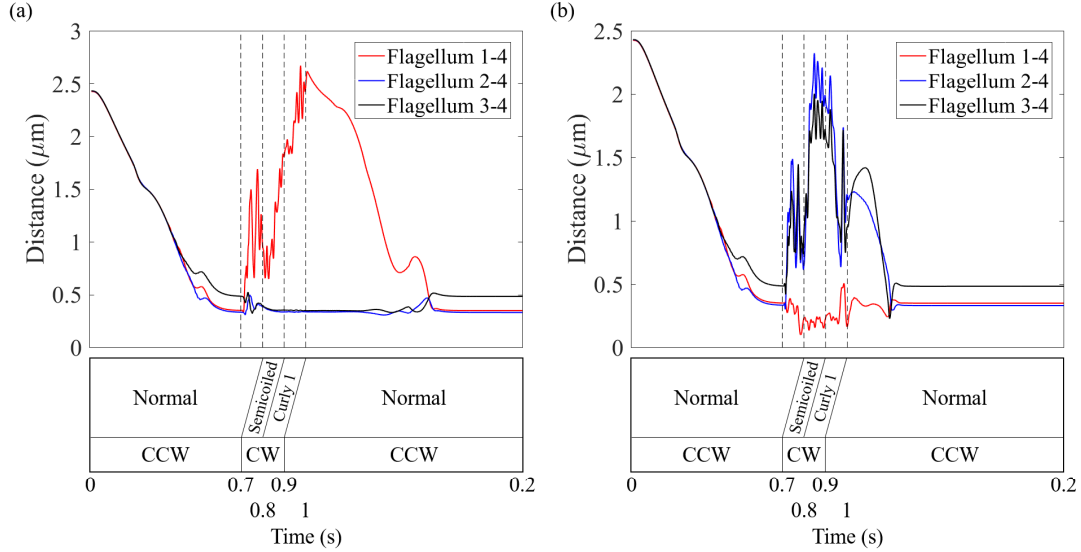
FIG. 14. (Color online) Distance from the tip of the central flagellum 4 to the tips of the flagella 1, 2, 3. The flagellum 4 is located in the center and the rest encircles it initially with equal distance from the flagellum 4.

(right), respectively. Flagella 1, 2, and 3 encircle flagellum 4 initially with equal distance 2.45 μm. The flagella start to form a bundle around $t = 0.5$ s and remain as a superflagellum until $t = 0.7$ s, which is indicated by the distances of the tips of the surrounding flagella from that of the central flagellum decreasing to be close to 0 in both cases. After initiating the motor reversal from CCW to CW and the chiral transformation of the flagellum 1 (left) or flagella 1 and 4 (right), the flagella start rapidly unbundling. As they unbundle, only the transformed flagellum 1 departs from the other flagella in the first case, and, similarly, a new bundle of transformed flagella 1 and 4 stay together and leave the original bundle in the second case. In both cases, two separate sets of bundles independently rotate during transition to curly 1 and eventually join each other upon the motor reversal back to CCW.

IV. SUMMARY AND CONCLUSIONS

The present model studies the hydrodynamic interaction of a single bacterial flagellum as well as multiple flagella, whose flagellar motors are tethered in space and whose rotation is transmitted to the filament via a flexible hook. As one or more motors switch to CW from CCW, the corresponding flagella undergo several transformations in a row, in which the flagella change their

23

helical shape from normal to semicoiled and then to curly 1 states. These dynamics put the flagella into two separate bundles, as observed in nature. These separate bundles rejoin together after another reversal of those motors from CW to CCW and the transformation of the associated filaments into normal state.

Unlike previous theoretical and computational studies, our model describes a sequence of three equilibrium states adopted from experimental data on flagellar polymorphism. Our results are in good agreement with previous computational work involving a single flagellum [26, 32]. The helical wave propagates from the motor to the free end while the flagellar motor turns CCW with a left-handed helix or CW with a right-handed helix, resulting in upward fluid pumping. However, there is a short period of reduced flow resulting from a large helical deformation from the normal state to the semicoiled state, or from the curly 1 state to the normal state, that is caused by motor reversal. Our results for multiple flagella provide quantitative information about how fluxes, which are relevant to the cell's swimming speed, and bundling efficiency depend on the number of flagella and the hook's properties, respectively. Our model yields a swimming speed that is independent of the number of flagella, and it suggests that the hook works as a universal flexible joint. These results are consistent with prior experimental data [7, 8]. Additionally, our simulations suggest a possible range of flagellar bundling, albeit in the absence of a cell body.

It has been experimentally reported that hook compliance is important in flagellar bundling [7, 8]. Our simulations have shown that there are constraints on both hook flexibility and hook length that determine whether the flagella can effectively bundle. If the hook is too rigid and short, then it only allows the adjacent flagella to form a bundle. To increase the range of scattered flagella for bundling, the hook is required to be sufficiently flexible and long. However, if the hook is too long and/or too flexible, the hook buckles and impairs flagellar bundling. With the appropriate hook stiffness and length, our simulation results still show the limited range of initial distance between flagella. We believe that the counter rotation of the cell body may improve this range of bundling.

A limitation of the present model becomes apparent when the flagella reconstitute a bundle after a cyclic event of transformations. During their transformations, the flagellar behavior of a real bacterium induces a large deflection of the cell body, and the new flagellar bundle is aligned with a new trajectory. However, our model in this work shows that the axis of the new flagellar bundle first demonstrates a certain amount of deviation from the axis of the original bundle but eventually returns to the same direction of the original flagellar bundle. This is purely because the

motors are clamped on the plane and do not have the freedom to reorient.

To capture the full dynamics of an *E. coil* as a free swimmer, the model needs to incorporate a cell body, which may also allow the study of the role of the cell body in reorientation. A comprehensive model equipped with a cell body and a flagellum may allow to measure actual swimming speed as well as the degree of course alteration depending on various geometrical properties and physical conditions.

A further improvement corresponding to the repulsive force between flagella is also required. Unlike the current model that makes use of artificial contact forces, the future model may use lubrication theory to resolve the flow geometry in the vicinity of flagellar bundle [39] and incorporate the electrostatic force since the surface of the flagella is negatively charged [40–43].

[1] N.C. Darnton and H.C. Berg, Biophys. J. **92** (2007)

[2] E. Lauga, Annu. Rev. Fluid Mech. **48** (2016).

[3] L. Turner, W. S. Ryu, and H. C. Berg, J. Bacteriol. **182**, 2793 (2000).

[4] S. M. Block, D. F. Blair, and H. C. Berg, Nature **338** (1989).

[5] T. S. Flynn and J. Ma, Biophys. J. **86**, (2004).

[6] A. Sen, R. K. Nandy, and A. N. Ghosh, J. of Electron Microscopy **53**, 3 (2013).

[7] H. C. Berg, R. A. Anderson, Nature **245** (1973).

[8] M.T. Brown, B.C. Steel, C. Silvestrin, D.A. Wilkinson, N.J. Delalez, C.N. Lumb, B. Obara, J.P. Armitage and R.M. Berry, J. Bacteriol. **194**, 13 (2012).

[9] H. Hotani, J. Mol. Biol. **156** (1982).

[10] R. M. Macnab and M. K. Ornston, J. Mol. Biol. **112**, 1 (1977).

[11] E. Hasegawa, R. Kamiya, and S. Asakura, J. Mol. Biol. **160**, 4 (1982).

[12] H. Hotani, Biosystems **12** (1980).

[13] R. Kamiya and S. Asakura, J. Mol. Biol. **106**, 1 (1976).

[14] M. Seville, T. Ikeda, and H. Hotani, FEBS Lett. **332**, 3 (1993).

[15] K. Shimada, R. Kamiya, and S. Asakura, Nature **254**, 332 (1975).

[16] C. R. Calladine, Nature **255** (1975).

[17] C.R. Calladine, J. Theor. Biol. **57**, 2 (1976).

[18] C. R. Calladine, J. Mol. Biol. **118**, 4 (1978).

[19] S. Asakura, Adv. Biophys. **1** (1970).

[20] H. Wada and R. R. Netz, Europhys. Lett. **82** (2008).

[21] R. Vogel and H. Stark, Eur. Phys. J. E **33** (2010).

[22] R. Vogel and H. Stark, Phys. Rev. Lett. **110** 158104 (2013).

[23] S.V. Srigiriraju and T.R. Powers, Phys. Rev. Lett. **94** 248101 (2005).

[24] R. E. Goldstein, A. Goriely, G. Huber, and C.W. Wolgemuth, Phys. Rev. Lett. **84**, 1631 (2000).

[25] D. Coombs, G. Huber, J.O. Kessler, and R. E. Goldstein, Phys. Rev. Lett. **89**, 118102 (2002).

[26] W. Ko, S. Lim, W. Lee, Y. Kim, H.C. Berg, C.S. Peskin, Phys. Rev. E **95**, 063106 (2017).

[27] J. J. Higdon, J. Fluid Mech. **94**, (1979).

[28] S. Lim, A. Ferent, X. S. Wang, and C. S. Peskin, SIAM J. on Scientific Computing **31**, 1 (2008).

[29] N. Chouaieb, A. Goriely, and J. H. Maddocks, Proc. Natl. Acad. Sci. **103**, 25 (2006).

[30] R. Cortez, SIAM J. on Scientific Computing **23**, 4 (2001).

[31] S. Olson, S. Lim, and R. Cortez, J. Comput. Phys. **238** (2013).

[32] S. Lim and C. S. Peskin, Phys. Rev. E **85**, 036307 (2012).

[33] W. Lee, Y. Kim, S. D. Olson, S. Lim, Phys. Rev. E **90**, 033012 (2014).

[34] H. C. Berg, Biochemistry **72** (2003).

[35] M. J. Kim, J. C. Bird, A. J. V. Parys, K. S. Breuer, and T. R. Powers, Proc. Natl. Acad. Sci. **100** (2003).

[36] Y. Man, W. Page, R. J. Poole, and E. Lauga, Phys. Rev. Fluids, **2**, 123101 (2017).

[37] N.C. Darnton, L. Turner, S. Rojevsky, and H.C. Berg, J. Bacteriol. **189**, 5 (2007).

[38] E. E. Riley, D. Das, and E. Lauga, Sci. Rep., **8** 10728 (2018).

[39] T.G. Fai and C.H. Rycroft, J. Comput. Phys. **356** (2018).

[40] H. C. Berg, Annual review of biophysics and bioengineering **4**, 1 (1975).

[41] J. S. Dickson, M. Koohmaraie, Applied and Environmental Microbiology **55**, 4, (1989).

[42] D. A. Lytle, E. W. Rice, C. H. Johnson, K. R. Fox, Applied and environmental microbiology, **65**, 7, (1999).

[43] J. W. McClaine, R. M. Ford, Applied and environmental microbiology **68**, 3, (2002).